Observation of a picosecond light-induced spin transition in polymeric nanorods

Supplementary Information

Marco Reinhard[1*], Kristjan Kunnus[1], Kathryn Ledbetter[2^], Elisa Biasin[1#], Diana Bregenholt Zederkof[3&], Roberto Alonso-Mori[1], Tim Brandt van Driel[1], Silke Nelson[1], Michael Kozina[1], Olaf J. Borkiewicz[4], Maciej Lorenc[5], Marco Cammarata[5], Eric Collet[5], Dimosthenis Sokaras[1], Amy A. Cordones[1], Kelly J. Gaffney[1*]

[1]SLAC National Accelerator Laboratory, Menlo Park, California 94025, USA

[2]Department of Physics, Stanford University, Stanford, California 94305, USA

[3]Department of Physics, Technical University of Denmark, 2800 Kongens Lyngby, Denmark

[4]X-ray Science Division, Argonne National Laboratory, Lemont, IL 60439, USA

[5]Univ Rennes, CNRS, IPR (Institut de Physique de Rennes) – UMR 6251, 35000 Rennes, France

Present addresses:

[^]Department of Physics, Harvard University, Cambridge, MA 02138, USA

[#]Physical Sciences Division, Pacific Northwest National Laboratory, Richland, Washington 99352, USA

[&]European XFEL GmbH, Holzkoppel 4, 22869 Schenefeld, Germany

[*]Corresponding authors:

E-mail: marcor@slac.stanford.edu, kgaffney@slac.stanford.edu

Supplementary Note 1: X-ray emission data analysis

Fit of the X-ray emission data and determination of the time-dependent HS fraction:

We have recorded time-dependent Fe Kβ main line XES difference maps $\Delta I_{XES}(t,E)$ for different excitation fluences (Supplementary Figure 1). For each fluence, we have then extracted the time-dependent HS fraction $\gamma(t)$ by fitting the measured area-normalized Fe Kβ main line difference spectra using the following expression:

$$\Delta I_{XES}(t,E) = \gamma(t) \cdot \left(I_{XES,S=2}(E) - I_{XES,S=0}(E) \right) \qquad (1)$$

Here, $I_{XES,S=0}(E)$ is the normalized $[Fe(2,2'\text{-bipyridine})_3]^{2+}$ singlet Fe Kβ main line XES reference spectrum and $I_{XES,S=2}(E)$ is the normalized $[Fe(phenanthroline)_2(NCS)_2]$ quintet reference spectrum both used from Zhang *et al.*[1]

To fit $\gamma(t)$ determined in the sub-picosecond range with an excitation fluence of 100 mJ/cm^2 (inset in Figure 2c), we have utilized the following fit function:

$$\gamma(t) = g(\sigma_{IRF}, t_0, t) \otimes \gamma_0 \cdot \theta_H(t - t_0) \cdot \left(e^{-\frac{t-t_0}{\tau_{long}}} - e^{-\frac{t-t_0}{\tau_0}} \right) \qquad (2)$$

Here, g is a normalized Gaussian instrument response function with $IRF\ FWHM = 2\sqrt{2ln2} \cdot \sigma_{IRF}$ and θ_H denotes the Heaviside step function. The decay constant τ_{long} is fixed to a large value. The fit yields a photoexcited HS fraction γ_0 = 0.72 ± 0.03, an IRF FWHM = 145 ± 70 fs, and the timescale for the formation of the HS state is fitted to τ_0 = 141 ± 55 fs. This timescale is comparable with LIESST timescales previously reported for different compounds.[1-2]

In a next step, we have then fitted $\gamma(t)$ for different excitation fluences up to ~70 picoseconds using the following phenomenological fit function:[3]

$$\gamma(t) = \sum_{j=0}^{1} \gamma_j \cdot \theta_H(t - t_j) \cdot \left(1 - e^{-(t-t_j)/\tau_j} \right) \qquad (3)$$

Here, t_j is the onset time and τ_j is the rise time of step j. To make the fit procedure more robust, we neglect the experimental time resolution (IRF FWHM ~ 145 fs), determined from the fit of the sub-picosecond data set. The onset and rise times of the molecular step (photodoping fraction) γ_0 due to LIESST are fixed to $t_0 = 0\ fs$ and $\tau_0 = 141\ fs$,[1-2, 4-7] respectively. This leaves the molecular and secondary spin conversion steps γ_0 and γ_1, the incubation period t_1 and the secondary spin conversion timescale τ_1 as fit variables. The fit results are tabulated in Supplementary Table 1. For the data collected with an excitation fluence of 25 mJ/cm^2, an unrestricted fit results in $\gamma_0 + \gamma_1 > 1$, indicating complete nanorod spin conversion within the probed range. To ensure $\gamma_0 + \gamma_1 \leq 1$, we have therefore fixed γ_1 to 0.72. For the data collected with 70 mJ/cm^2 and 100 mJ/cm^2, no incubation period is resolved, and we have therefore fixed t_1 to zero to improve the fit stability. We note that we have collected two independent data sets with an excitation fluence of 100 mJ/cm^2, in the sub-picosecond range and an extended ~70 ps range. For both data sets, the fitted molecular step magnitudes γ_0 are in good agreement. For 10 mJ/cm^2,

the total HS fraction remains well below one, while at higher fluences HS fractions near unity are achieved. No reliable trend in the conversion rates τ_1 is observed for different photodoping fractions. All fits are shown in Figure 2c.

Excitation fluence (mJ/cm^2)	γ_0 (-)	γ_1 (-)	$\gamma_0 + \gamma_1$ (-)	t_1 (ps)	τ_1 (ps)
10	0.12 ± 0.01	0.13 ± 0.04	0.25 ± 0.04	29 ± 4	12 ± 11
25	0.28 ± 0.01	0.72 (fixed)	1.00 (fixed)	22 ± 2	43 ± 3
35	0.42 ± 0.01	0.54 ± 0.04	0.96 ± 0.04	17 ± 1	22 ± 4
70	0.60 ± 0.02	0.40 ± 0.03	1.00 ± 0.04	0 (fixed)	22 ± 5
100	0.70 ± 0.03	0.29 ± 0.03	0.99 ± 0.03	0 (fixed)	5 ± 1

Supplementary Table 1: Extracted parameters from the fit of the HS fraction $\gamma(t)$ determined from the XES difference maps. Uncertainties represent 95% confidence bounds.

Extraction of the photodoping threshold γ_{th}: Immediately following photoexcitation and before the onset of nonlinear, secondary spin conversion processes, the HS fraction exhibits an exponential decay profile $\gamma_0'(z)$ as a function of the liquid sample jet depth z (Figure 2d and Supplementary Figure 2).

$$\gamma_0'(\mathrm{z}) = \frac{\alpha \mathrm{d}}{1-\mathrm{e}^{-\alpha \mathrm{d}}} \gamma_0 \mathrm{e}^{-\alpha \mathrm{z}} \qquad (4a)$$

$$\alpha = \log(10) \cdot \varepsilon_{266nm} \cdot \mathrm{c} \qquad (4b)$$

$\varepsilon_{266nm} \approx 6923\ M^{-1} \cdot cm^{-1}$, $c \approx 12.5\ mM$ and $d = 50\ \mu m$ are the extinction coefficient, Fe-concentration of the nanoparticle suspensions and nominal sample jet thickness, respectively. For excitation fluences in the range 25–100 mJ/cm^2, $\gamma_0 + \gamma_1$ approaches one at longer delays, which indicates that the nanorods convert to the HS phase within the entire probed jet region. The excitation fraction achieved at the maximum probed jet depth d therefore provides an upper bound on the photodoping threshold that needs to be exceeded to achieve nanorod switching. The extracted upper bounds for fluences in the 25–100 mJ/cm^2 range are indicated in Supplementary Figure 2.

For an excitation fluence of 10 mJ/cm^2, $\gamma_0 + \gamma_1 \approx 0.25$ and the photodoping threshold can be determined using the fitted values γ_0 and γ_1 as follows. We first assume that at sufficiently long delays t_l when the nanorods photoexcited above the threshold $\gamma_{th} = \gamma_0'(z_{th})$ have converted to the HS phase but prior to the subsequent relaxation of the HS phase, the HS fraction saturates at $\gamma(t_l) \equiv \gamma_0 + \gamma_1$. Here, we also assume that nanorods photoexcited below the threshold approximately retain their photodoping fraction. This approximation is justified as molecular HS state lifetimes typically exceed one nanosecond in solution[8] while in the solid phase, a negative feedback of non-switched neighboring lattice sites can somewhat accelerate HS-LS recovery.[9] The observed HS fraction $\gamma(t_l)$ can also be expressed as

$$\gamma(t_l) \equiv \gamma_0 + \gamma_1 = \frac{1}{d}\int_0^d dz\, \gamma'(z, t_l) = \frac{1}{d}\int_0^{z_{th}} dz\, \gamma_s'(z, t_l) + \frac{1}{d}\int_{z_{th}}^d dz\, \gamma_n'(z, t_l) \qquad (5)$$

where we have split the integral into regions of switching and non-switching particles defined via:

$$\gamma'(z,t_l) = \begin{cases} \gamma_s'(z,t_l) \equiv 1, \ z \geq z_{th} \\ \gamma_n'(z,t_l) \equiv \gamma_0'(\mathrm{z}), \ z < z_{th} \end{cases} \qquad (6)$$

Combining equations 5 and 6, we then obtain the following equation for z_{th} that can be solved using the fitted values for γ_0 and γ_1 from Supplementary Table 1:

$$\gamma_0 \left(\frac{1-e^{-\alpha z_{th}}}{1-e^{-\alpha d}}\right) - \frac{z_{th}}{d} + \gamma_1 = 0 \qquad (7)$$

For the 10 mJ/cm^2 data set, we find $z_{th} = 8 \pm 3\ \mu m$. $\gamma_{th} = \gamma_0'(z_{th}) = 0.16 \pm 0.01$, therefore, provides an estimate of the photodoping threshold required to switch a particle completely from the LS to the HS phase. To estimate the uncertainty in the photodoping threshold, Equation 7 was solved 5000 times for z_{th} and γ_{th} using sets of input parameters (ε_{266nm}, c, d, γ_0, γ_1) that were randomly chosen around the measured values by assuming normal distributions. For the widths of these uncertainties, we assumed 1000 $M^{-1} \cdot cm^{-1}$ for the extinction coefficient at 266 nm, 2.5 mM for the Fe-concentration of the nanorod suspensions and 15 µm for the jet thickness. Uncertainties for γ_0, γ_1 were directly taken from Supplementary Table 1. The uncertainties of z_{th} and γ_{th} were then estimated as the standard deviation of the 5000 values.

Excitation fluence considerations: Supplementary Figure 3 shows the photodoping fraction γ_0 from Supplementary Table 1 as a function of the photoexcitation fluence.

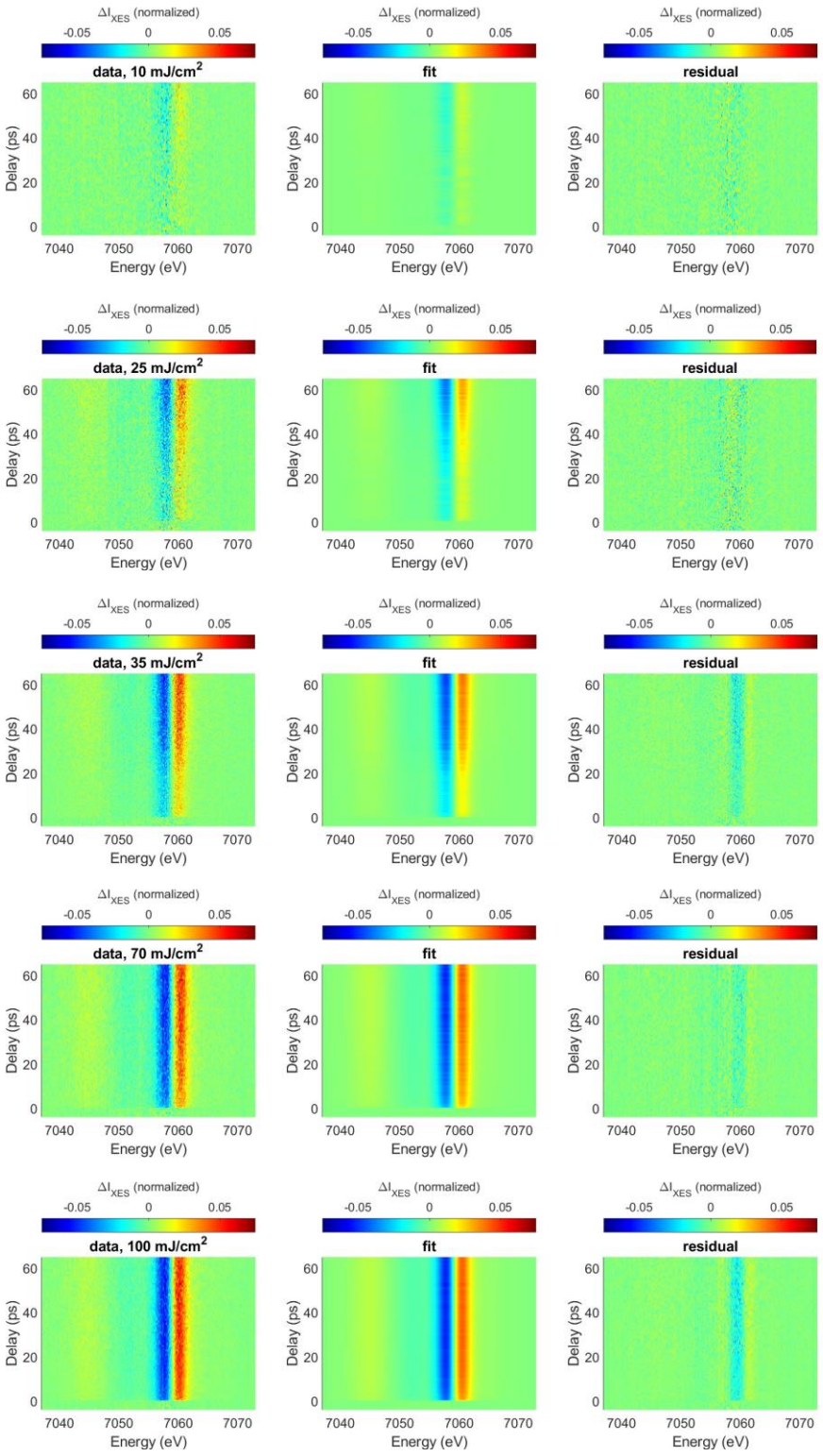

Supplementary Figure 1: Time-dependent Fe Kβ main line XES difference maps for different excitation fluences (left column). The middle column shows the fitted maps based on Supplementary Equation 1. The right column shows the fit residuals.

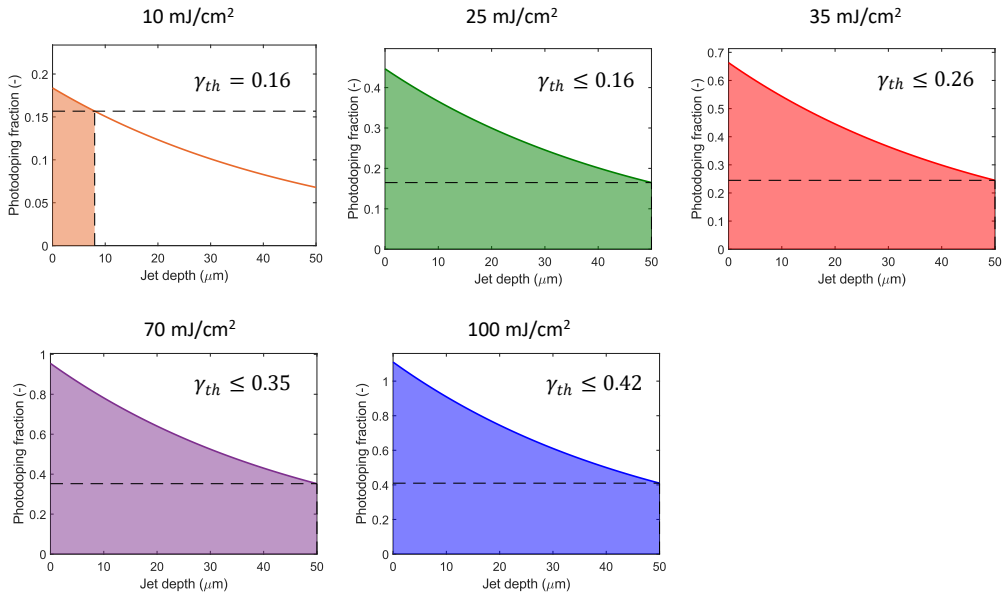

Supplementary Figure 2: Photodoping fraction $\gamma_0'(z)$ as a function of the liquid sample jet depth z. For fluences in the 25-100 mJ/cm^2 range, the photodoping fraction at the largest jet depth d exceeds the photodoping threshold for nanorod switching. At 10 mJ/cm^2, the threshold is at $z_{th} = 8 \pm 3\ \mu m$ and $\gamma_{th} = \gamma_0'(z_{th}) = 0.16 \pm 0.01$.

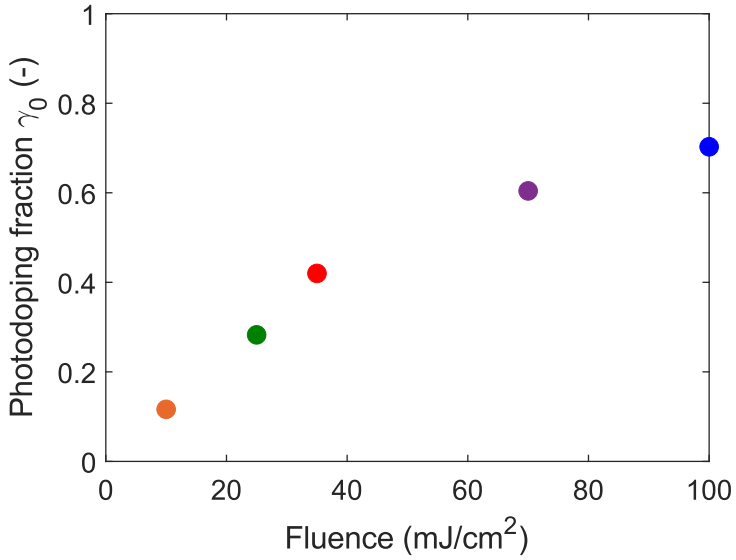

Supplementary Figure 3: Fitted photodoping fraction γ_0 extracted for different excitation fluences. Values are reported in Supplementary Table 1.

Supplementary Note 2: X-ray solution scattering data analysis

The measured time-dependent XSS difference maps are shown in Supplementary Figure 4 for different excitation fluences. The significant size-related broadening of the diffraction peaks combined with the relatively large number of peaks present in the experimentally measured Q-range 0.5 – 4.5 Å^{-1} does not permit an accurate extraction of the time-dependent lattice spacings using a Rietveld refinement or profile matching procedure. We therefore opt for a more qualitative discussion of the time evolution of diffraction features associated with the nanorod lateral and longitudinal directions.

First, we note that the scaled difference between the powder X-ray diffraction (XRD) HS and LS curves measured at thermal equilibrium resembles the time resolved XSS difference curves (Supplementary Figure 5) but does not account for all the observed features which indicates that the time resolved XSS differences exhibit structural sensitivity beyond the HS/LS phase composition. The crystal structure of $[Fe(Htrz)_2(trz)](BF_4)$ has previously been analyzed by Grosjean et al.[10] which we use to discuss the observed features in our measurements. In the momentum transfer range Q ≤ 2 Å^{-1} the thermal equilibrium XRD curves exhibit four separated peak features (Figure 3b). The first feature around ~0.76 Å^{-1} consists of the (200) and (101) reflections and the second feature around ~1.3 Å^{-1} primarily stems from the (301) and (002) reflections. The XSS difference signal in the Q-range < 1.5 Å^{-1} therefore reflects changes orthogonal to the polymer axis but is insensitive to changes parallel to the polymer axis. The XRD feature around ~1.73 Å^{-1} predominantly arises from the (410) and (212) reflections and the dominant contribution to the separated feature around ~1.87 Å^{-1} stems from the (121) reflection with a minor contribution from the (220) reflection which we neglect in the following analysis.

The total time resolved XSS difference signal can be expressed as:

$$\Delta S(Q,t) = \Delta S_{NP}(Q,t) + \Delta S_{cage}(Q,t) + \Delta S_{solvent}(Q,t) \quad (8)$$

The nanorod heat dissipation analysis discussed below and visualized in Supplementary Figure 10 indicates that $\Delta S(Q,t) \approx \Delta S_{NP}(Q,t) = S_{NP}(Q,t) - S_{NP}^{LS}(Q)$ within the first ~100 ps. However, since Fe-triazole nanorods were dispersed in ethanol at micromolar concentrations, the radially integrated, time-resolved total XSS signal is dominated by the known ethanol liquid peak,[11] and therefore the nanocrystal total scattering curve $S_{NP}^{LS}(Q)$ could not be extracted from the time resolved XSS experiments. To extract $S_{NP}(Q,t)$, we have therefore used $S_{NP}^{LS}(Q) = \alpha \cdot S_{XRD}^{LS}(Q)$, where S_{XRD}^{LS} is the independently measured room temperature powder XRD curve. The scaling factor α was determined by fitting the measured thermal equilibrium HS-LS difference ($\Delta S_{XRD}^{HL} = S_{XRD}^{HS} - S_{XRD}^{LS}$) to the XSS difference signal $\Delta S(Q,t)$ at fluences and time delays where the XES measurement indicates nearly complete HS conversion (Figure 2c). This fit also considers a scaling factor for the Q-axis to account for differences in calibration between the femtosecond XSS and steady-state XRD measurements. With this, the nanocrystal total scattering curves were extracted using:

$$S_{NP}(Q,t) \approx \Delta S(Q,t) + \alpha \cdot S_{XRD}^{LS}(Q) \quad (9)$$

We then independently fitted the different peak features of $S_{NP}(Q,t)$ using a sum of pseudo-Voigt functions defined as:

$$V_p(Q,t) = \sum a_i(t) \cdot V_{p,i}(Q,t) \qquad (10)$$

The pseudo-Voigt functions are defined via:

$$V_{p,i}(Q,t) = \eta_i \cdot L_i(Q,t) + (1-\eta_i) \cdot G_i(Q,t) \qquad (11a)$$

$$L_i(Q,t) = \frac{\gamma_i}{\pi((Q-Q_i)^2+\gamma_i{}^2)} \qquad (11b)$$

$$G_i(Q,t) = \frac{1}{\sqrt{2\pi}\sigma_i} e^{-\frac{(Q-Q_i)^2}{2\sigma_i{}^2}} \qquad (11c)$$

$$\eta_i = 1.36603 \cdot \left(\frac{w_{L,i}}{w_{tot,i}}\right) - 0.47719 \cdot \left(\frac{w_{L,i}}{w_{tot,i}}\right)^2 + 0.11116 \cdot \left(\frac{w_{L,i}}{w_{tot,i}}\right)^3 \qquad (11d)$$

$$w_{L,i} = 2\gamma_i \qquad (11e)$$

$$w_{G,i} = 2\sqrt{2\log(2)}\sigma_i \qquad (11f)$$

$$w_{tot,i} = \left(w_{G,i}{}^5 + 2.69269 \cdot w_{G,i}{}^4 w_{L,i} + 2.42843 \cdot w_{G,i}{}^3 w_{L,i}{}^2 + 4.47163 \cdot w_{G,i}{}^2 w_{L,i}{}^3 + 0.07842 \cdot w_{G,i}{}^1 w_{L,i}{}^4 + w_{L,i}{}^5\right)^{1/5} \qquad (11g)$$

For each time delay, we therefore fit a set of amplitudes $a_i(t)$, widths $\sigma_i(t)/\gamma_i(t)$, and peak positions $Q_i(t)$. For the (200)/(101) and (301)/(002) peaks, a singular value decomposition (SVD) indicates that the signal predominantly arises from a global amplitude change and a global peak shift, but no changes occur that would allow distinguishing two separate diffraction peaks (Supplementary Figures 6-7). We therefore use a single pseudo-Voigt function to fit the time-dependence of the diffraction signal in the range 0.6 – 0.9 Å^{-1}. To further reduce the number of fit parameters, we assume $\sigma_i = \gamma_i$. Analogously, the (301)/(002) peak feature is fitted with a single pseudo-Voigt function in the Q-range 1.10 – 1.43 Å^{-1} with $\sigma_i = \gamma_i$. To extract the peak associated with the (121) reflection, we fit the Q-range 1.47 – 1.98 Å^{-1} where the (410), (212) and (121) reflections contribute to the observed scattering intensity.[10] For this Q-range, we therefore utilize a sum of three pseudo-Voigt functions. Again, we set $\sigma_i = \gamma_i$. As the width is expected to predominantly reflect the particle linear dimensions (Supplementary Note 3), we then further assume that $\sigma_1 = \sigma_2$ for the (410) and (212) reflections. A separate width σ_3 is used for the (121) reflection as the nanorods are larger along the *b*-axis. For all fits, a linear background was subtracted prior to the fit. The extracted time-dependent peak positions were normalized to the fitted difference in peak positions between the thermal equilibrium HS and LS XRD curves. Fits for the extracted time evolution of the peak features are shown in Supplementary Figures 8-9 for the 35 mJ/cm^2 and 70 mJ/cm^2 data sets.

An extended analysis of the time evolution of the nanorod lattice spacings is provided in Supplementary Note 5.

Nanorod heat dissipation into the solvent: We quantify the photoinduced change in solvent temperature using a previously reported procedure.[11-13] For the highest excitation fluence (100 mJ/cm^2) transient XSS curves were collected at delays up to 550 nanoseconds (Supplementary Figure 10a). The measured difference scattering curves ΔS are normalized to reflect a liquid unit cell containing the appropriate number of ethanol molecules per Fe-center and fitted in the Q-range 0.5 – 2.825 Å^{-1} as a linear combination of the transient difference signal due to the nanorod structural response ΔS_{NP}, and the solvent contribution $\Delta S_{solvent}$ that comprises the scaled ethanol heat and density differentials:

$$\Delta S(Q,t) \approx \Delta S_{NP}(Q,t) + \frac{\partial S(Q)}{\partial T}\Big|_{\rho_{EtOH}} \cdot \Delta T_{EtOH}(t) + \frac{\partial S(Q)}{\partial \rho}\Big|_{T_{EtOH}} \cdot \Delta \rho_{EtOH}(t) \qquad (12)$$

The ethanol differentials for temperature and density changes (Supplementary Figure 10b) have previously been determined by Kjaer *et al.*[11] and $\Delta S_{NP}(Q,t)$ is the transient signal due to the nanoparticle structural response. As shown in Supplementary Figure 10a, reasonable agreement between the experimental and fitted curves is achieved despite neglecting the cage term ΔS_{cage} from Supplementary Equation 8. For this excitation fluence (100 mJ/cm^2), XES indicates nearly complete LS to HS conversion in the 50-100 ps range and the transient signal in this time delay range resembles the scaled difference of the scaled HS/LS powder XRD curves measured at thermal equilibrium. Deviations between the time-dependent XSS differences and the HS/LS difference were discussed in the previous section and are shown in Supplementary Figure 5. Here, we neglect these deviations and therefore approximate $\Delta S_{NP}(Q,t) \approx \gamma_{XSS}(t) \cdot \Delta S_{XRD}^{HL}$. The time-dependent magnitude of the XRD difference signal γ_{XSS} is therefore taken as a proxy for the HS fraction which is justified given the relatively small changes in signal shape at different HS fractions compared to the solvent heat and density differentials. A comparison between the fitted approximate HS fraction $\gamma_{XSS}(t)$ and the HS fraction $\gamma(t)$ derived from the XES measurement shows reasonable agreement. Fitting the transient signal between 12 ps and 550 ns therefore yields $\gamma_{XSS}(t)$, $\Delta T_{EtOH}(t)$ and $\Delta \rho_{EtOH}(t)$ as shown in Supplementary Figures 10c-d).

In the 12–100 ps range, the ethanol temperature increases by $\Delta T_{EtOH} \approx 0.62 \pm 0.14$ K as determined by averaging the data points from Supplementary Figure 10c. The ethanol density change remains negligible (Supplementary Figure 10d). The maximum solvent temperature increase that could result from photon absorption at the molecular sites within a nanorod can be estimated using $\Delta T_{max} = \frac{E_{tot}}{C_{V,EtOH}} = 2.6 \pm 0.6$ K. Here, E_{tot} represents the total energy deposited and $C_{V,EtOH}$ is the molar heat capacity of ethanol at constant volume. This estimate is consistent with the observed trend of the fitted temperature evolution shown in Supplementary Figure 10c. Therefore, a fraction of 0.24 ± 0.08 of the excess energy dissipates into the solvent during the first 100 ps, while ~76% remains trapped within the nanorods.

Estimated nanorod temperature jump: To estimate the increase in nanorod temperature that results from photo-excitation at the switching threshold, we numerically solve the following equation from Park and van der Veen:[14]

$$\left((1-\gamma)C_p^{LS}+\gamma C_p^{HS}\right)\frac{\partial T}{\partial t}+\Delta H\frac{\partial \gamma}{\partial t}=\frac{d\tilde{Q}}{dt} \qquad (13)$$

For the time-dependent nanoparticle heat $\tilde{Q}$, we assume an exponential rise following photo-doping combined with an exponential decay reflecting heat dissipation into the solvent:

$$\tilde{Q}(t)=G(\sigma_{IRF},t_0,t)\otimes\gamma_0\cdot\frac{hc}{\lambda}\cdot\theta(t-t_0)\cdot(e^{-t/\tau_{decay}}-e^{-t/\tau_{rise}}) \quad (14)$$

At the photo-switching threshold, $\gamma(t)$ is approximated by a step function with magnitude γ_0 convoluted with the Gaussian instrument response function G.

Since we do not have a measurement of the heat capacities of $[Fe(Htrz)_2(trz)](BF_4)$, we estimate the specific heat capacities at constant pressure of the LS and HS phases ($C_p^{LS}\approx 1.0\ kJ\cdot mol^{-1}\cdot K^{-1}, C_p^{HS}\approx 1.0\ kJ\cdot mol^{-1}\cdot K^{-1}$) based on heat capacities reported by Roubeau et al.[15] for similar one-dimensional triazole-bridged Fe(II) ST materials. Moreover, we use $\Delta H\approx 27.8\ kJ\cdot mol^{-1}$ determined for $[Fe(Htrz)_2(trz)](BF_4)$ by Kroeber et al.[16] and Roubeau et al.[15] and vary the nanorod heating timescale τ_{rise} in a realistic range between 1 ps and 30 ps. We then find that at the photodoping threshold $\gamma_{th}=0.16\pm0.01$, the nanoparticle temperature increases by $60\pm15\ K$. Here, the uncertainty is estimated by considering uncertainties of $\pm0.2\ kJ\cdot mol^{-1}\cdot K^{-1}$ for the heat capacities, $\pm0.5\ kJ\cdot mol^{-1}$ for the enthalpy difference, the reported uncertainty for γ_{th} and considering the effect of varying τ_{rise} in the 1–30 ps range. For each value of τ_{rise}, the exponential timescale τ_{decay} for heat dissipation from the nanorods to the solvent is chosen such that the nanoparticle heat in the 12-100 ps range amounts to ~76% of the initially deposited excess energy, as experimentally observed from the fit of the XSS difference data. Consequently, at the photo-switching threshold, the nanorod temperature raises to ~353 K, close to $T_{\uparrow}\approx 361\ K$, the thermal transition temperature estimated for the Zn-doped compound $[Fe_{1-x}Zn_x(Htrz)_2(trz)](BF_4)$ from Lefter et al.[17] for a Zn-doping fraction of 16%.

For this analysis we have assumed $\phi_{LIESST}\approx 1$ for the LIESST quantum yield. $\phi_{LIESST}<1$ would imply that the amount of energy deposited in the nanorods is higher and consequently the estimated nanorod temperature increase to ~353 K at the photodoping threshold γ_{th} should be interpreted as a lower limit. The XES data collected using an excitation fluence of 100 mJ/cm^2 shows that $\phi_{LIESST}\gtrsim 0.70$.

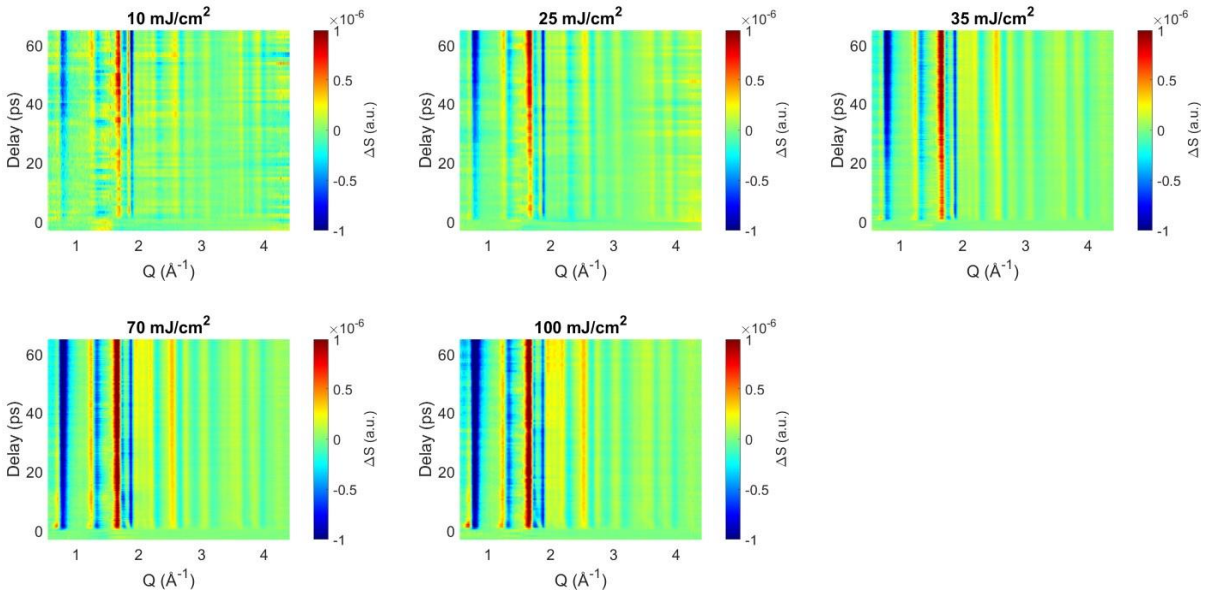

Supplementary Figure 4: Time-dependent XSS difference maps measured for different excitation fluences.

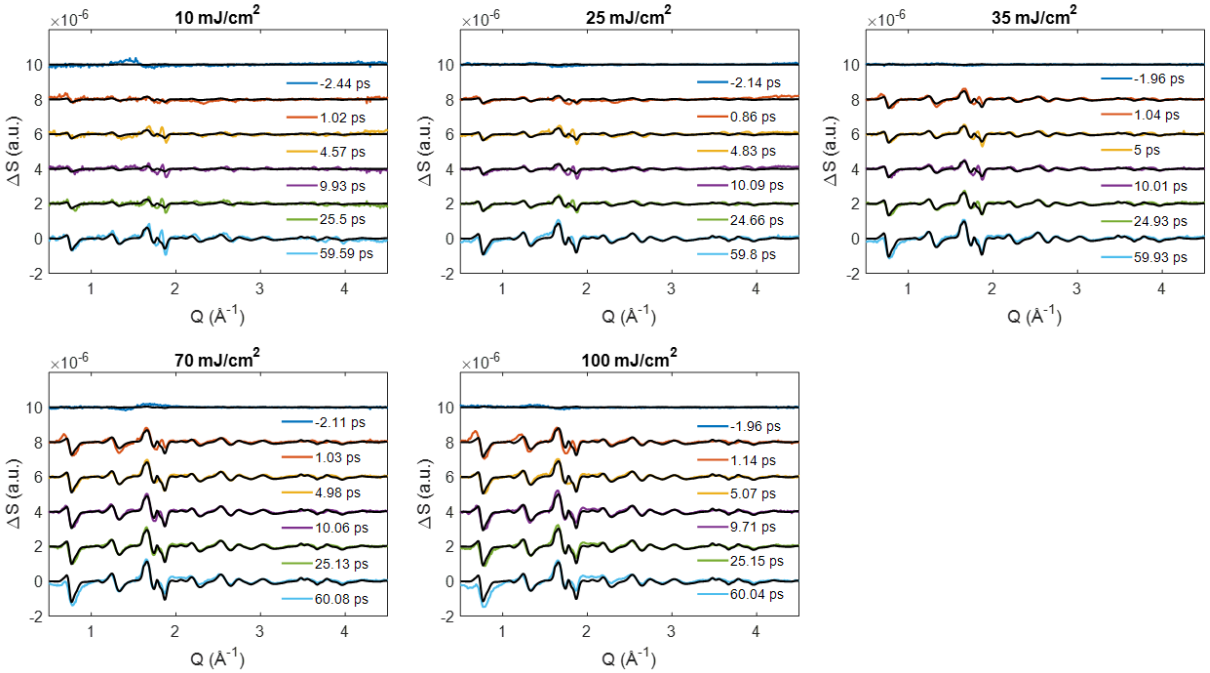

Supplementary Figure 5: Time dependent XSS difference curves at different time delays and different excitation fluences. Black lines represent the HS-LS difference $\Delta S_{XRD}^{HL}(Q)$ from the XRD measurements multiplied by a fitted scaling factor.

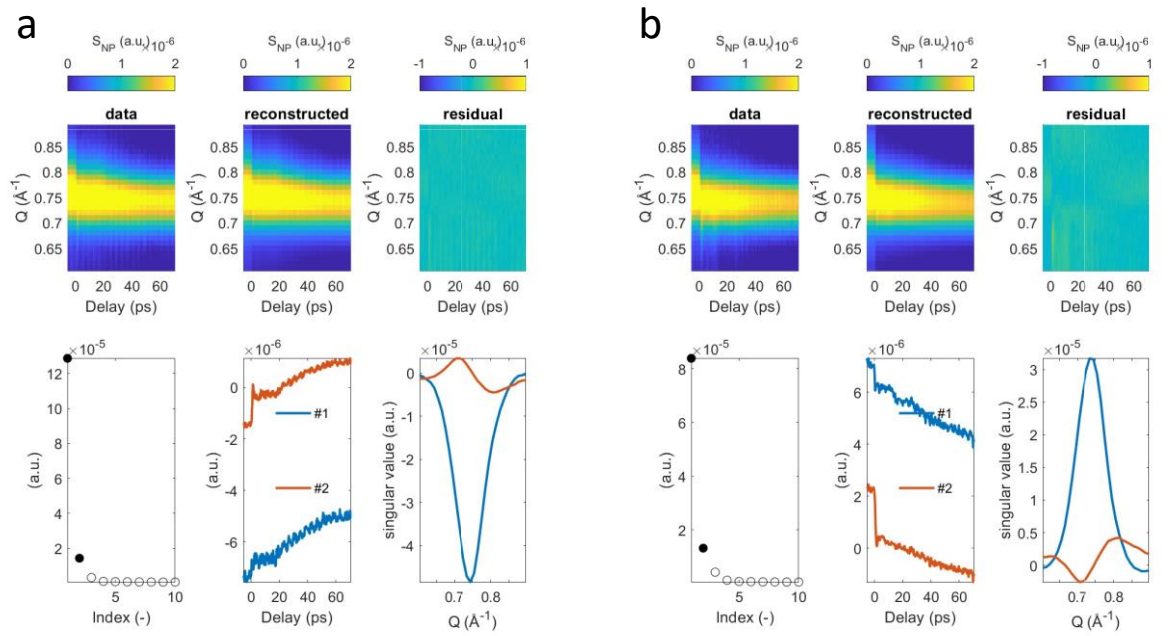

Supplementary Figure 6: SVD of the time-dependent nanorod total scattering curves $S_{NP}(Q,t)$ in the Q-range ~0.60-0.90 Å^{-1}. Data shown in (a, b) has been collected using an excitation fluence of 35/70 mJ/cm^2, respectively. The top left inset shows $S_{NP}(Q,t)$ constructed from the difference map $\Delta S(Q,t)$ and the XRD curve of the LS phase $S_{XRD}^{LS}(Q)$ using Supplementary Equation 9. The top middle inset shows the reconstructed data using the first two SVD components. The top right inset shows the residual. The lower left inset shows the singular values, the lower middle inset shows the first two temporal components of the SVD, and the lower right inset shows the first two Q-dependent components of the SVD, reflecting a global amplitude change and shift, respectively.

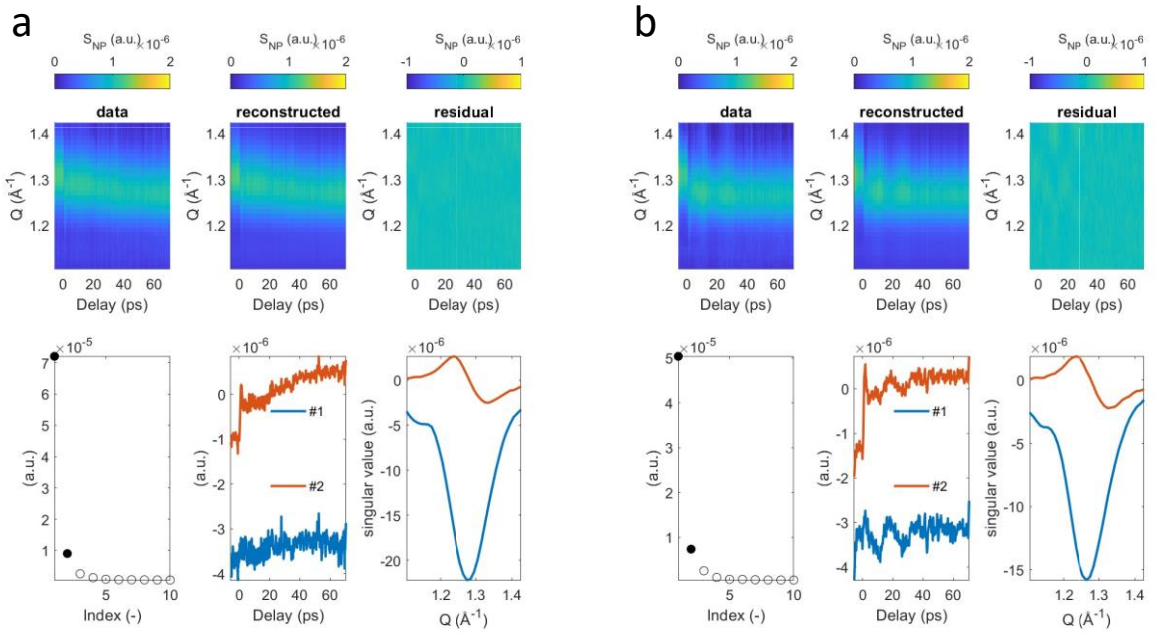

Supplementary Figure 7: SVD of the time-dependent nanorod total scattering curves $S_{NP}(Q,t)$ in the Q-range ~1.10-1.43 Å^{-1}. Data shown in (a, b) has been collected using an excitation fluence of 35/70 mJ/cm^2, respectively. The top left inset shows $S_{NP}(Q,t)$ constructed from the difference map $\Delta S(Q,t)$ and the XRD curve of the LS phase $S_{XRD}^{LS}(Q)$ using Supplementary Equation 9. The top middle inset shows the reconstructed data using the first two SVD components. The top right inset shows the residual. The lower left inset shows the singular values, the lower middle inset shows the first two temporal components of the SVD, and the lower right inset shows the first two Q-dependent components of the SVD, reflecting a global amplitude change and shift, respectively.

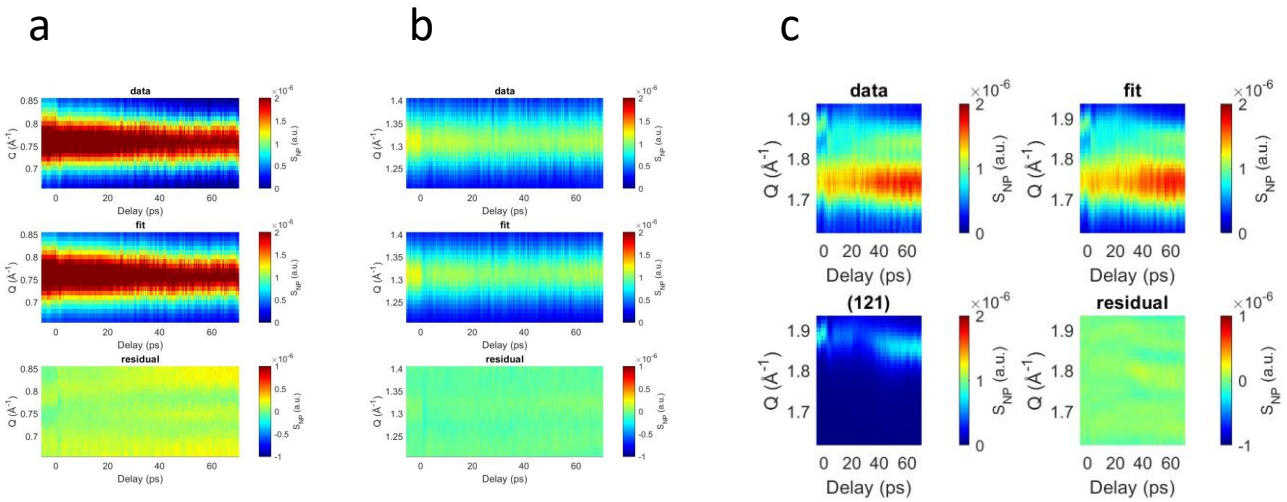

Supplementary Figure 8: Extraction of the peak positions of the time-dependent nanorod total scattering signal $S_{NP}(Q,t)$ observed in the Q-range ~0.60-1.98 Å^{-1}. The data was collected using an excitation fluence of 35 mJ/cm^2. The resulting time dependent peak positions are shown in Figure 3c. (a) The top inset shows $S_{NP}(Q,t)$ in the Q-range ~0.60-0.90 Å^{-1}, constructed using Supplementary Equation 9. The peak contains the (101) and (200) reflections. The middle inset shows the fit result using Supplementary Equation 10 with a single pseudo-Voigt peak. The bottom inset shows the residual. (b) The top inset shows $S_{NP}(Q,t)$ in the Q-range ~1.10-1.43 Å^{-1}, constructed using Supplementary Equation 9. The peak contains the (301) and (002) reflections. The middle inset shows the fit result using Supplementary Equation 10 with a single pseudo-Voigt peak. The bottom inset shows the residual. (c) The upper left inset shows $S_{NP}(Q,t)$ in the Q-range 1.47-1.98 Å^{-1}. The upper right inset shows the fit using three pseudo-Voigt peaks for the (410), (212) and (121) reflections. The lower left inset shows the fitted contribution of the (121) reflection. The lower right inset shows the fit residual.

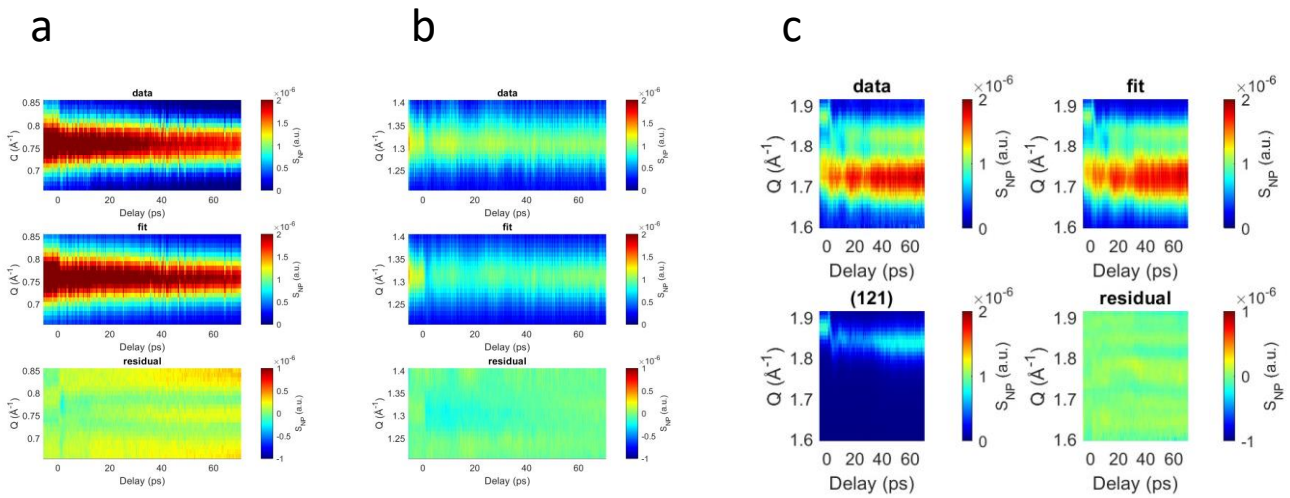

Supplementary Figure 9: Extraction of the peak positions of the time-dependent nanorod total scattering signal $S_{NP}(Q,t)$ observed in the Q-range ~0.60-1.98 Å^{-1}. The data was collected using an excitation fluence of 70 mJ/cm^2. The resulting time dependent peak positions are shown in Figure 3d. (a) The top inset shows $S_{NP}(Q,t)$ in the Q-range ~0.60-0.90 Å^{-1}, constructed using Supplementary Equation 9. The peak contains the (101) and (200) reflections. The middle inset shows the fit result using Supplementary Equation 10 with a single pseudo-Voigt peak. The bottom inset shows the residual. (b) The top inset shows $S_{NP}(Q,t)$ in the Q-range ~1.10-1.43 Å^{-1}, constructed using Supplementary Equation 9. The peak contains the (301) and (002) reflections. The middle inset shows the fit result using Supplementary Equation 10 with a single pseudo-Voigt peak. The bottom inset shows the residual. (c) The upper left inset shows $S_{NP}(Q,t)$ in the Q-range 1.47-1.98 Å^{-1}. The upper right inset shows the fit using three pseudo-Voigt peaks for the (410), (212) and (121) reflections. The lower left inset shows the fitted contribution of the (121) reflection. The lower right inset shows the fit residual.

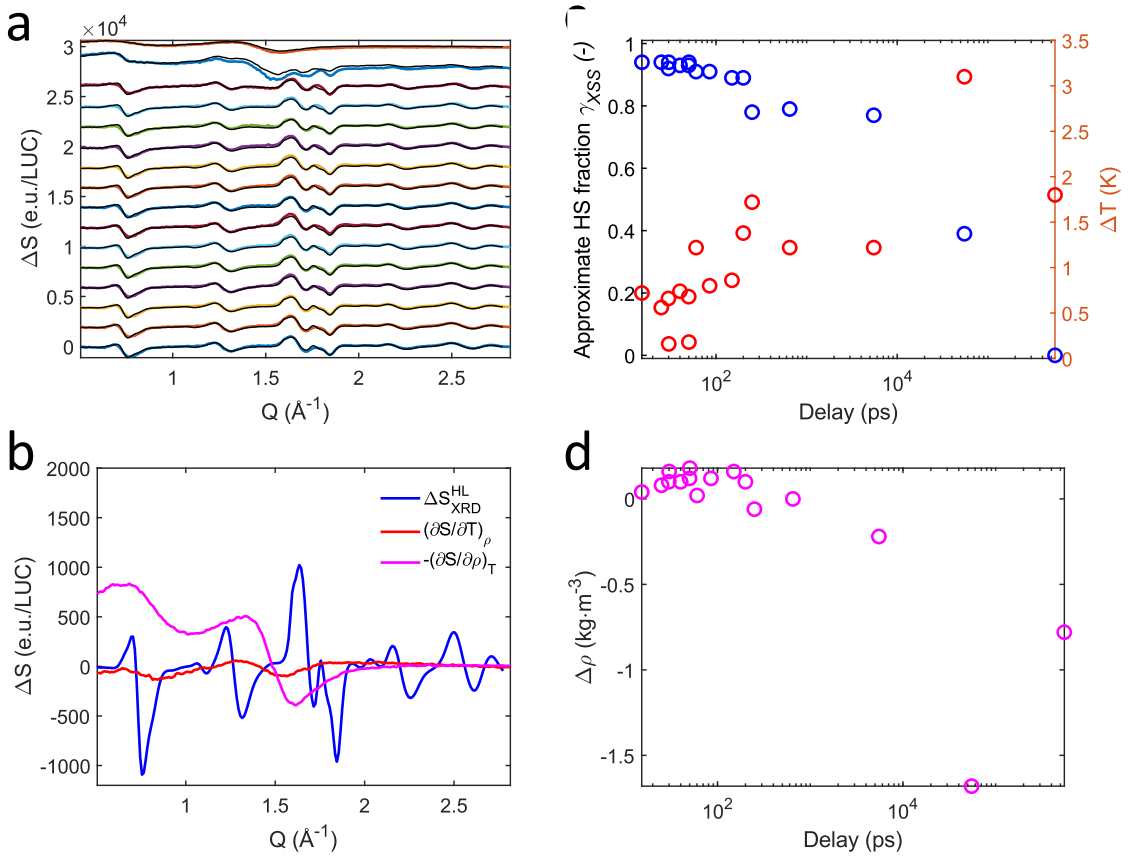

Supplementary Figure 10: Excess energy dissipation analysis for photoexcitation with a fluence of 100 mJ/cm^2. (a) Transient XSS difference curves $\Delta S(Q,t)$ at different time delays. Fits using Supplementary Equation 12 are represented by the black lines. (b) Reference curves used to fit the data shown in (a): The blue curve is the XRD HS-LS difference curve $\Delta S^{HL}_{XRD}(Q)$, the red and purple curves represent the ethanol heat and density differentials from Kjaer *et al.*[11] representing a temperature increase of 1 K and a density decrease of 1 kg/m^3, respectively. (c) Fitted approximate HS fraction and ethanol temperature increase. (d) Fitted ethanol density change.

Supplementary Note 3: Nanoparticle synthesis and characterization

Synthesis, size, and shape analysis: Fe-triazole nanorods were synthesized based on previously reported procedures.[18-20] We first separately dissolved 0.505 g $Fe(BF_4)_2 \cdot H_2O$ and 0.31 g 1,2,4-1H-Triazole each in 1.5 ml deionized water. We then prepared two identical solutions of 6.73 g sodium dioctyl sulfosuccinate (surfactant) dissolved in 50 ml *N*-octane. The iron/ligand solutions were subsequently added to the surfactant solutions and stirred vigorously for ~2.5 hours until the initially cloudy microemulsions appeared transparent. Both suspensions were subsequently mixed and stirred for another 0.5 hours, allowing for micellar exchange and nanoparticle growth. 30 ml of acetone was then added per 10 ml of the purple nanoparticle suspensions and the mixture was centrifuged at 11 krpm for 10 minutes to separate nanoparticles from the supernatant. Nanoparticles were then immediately resuspended in ~10 ml ethanol per 10 ml of the original *N*-octane suspensions using an ultrasound bath. Thus, the Fe-concentration was maintained at ~10-15 mM. The UV-visible absorption spectrum (Supplementary Figure 11a) exhibits a strong peak below 400 nm and a very weak transition centered around ~530 nm. Generally, these suspensions remained stable for several weeks. All samples were prepared a few days before the measurements at the LCLS. Nanoparticle dimensions were estimated based on a line width analysis of the temperature dependent XRD curves measured at beamline 11-ID-B of the APS, transmission electron microscopy (TEM) images recorded at the Stanford Nano Shared Facilities, and a comparison with simulations using the Debye scattering equation. Nanoparticle shape analysis based on measured line widths[21-22] was performed using the Scherrer formula for the crystal thicknesses t_{hkl} in different directions defined by the Miller indices (hkl):

$$t_{hkl} = \frac{K\lambda}{B_{hkl}\cos\theta_{hkl}} \qquad (15)$$

K is the Scherrer constant, $\lambda = 0.2113$ Å is the wavelength, B_{hkl} is the integral breadth (integral of the fitted peak divided by the peak maximum) in radians for each XRD peak and θ_{hkl} is the peak position. The B_{hkl} were determined from fitting multiple overlapping diffraction peaks with known Miller indices using pseudo-Voigt functions. The Scherrer constant is approximated as $K \approx 0.9$. Since the nanoparticles are small, instrument broadening is neglected, and it is assumed that the measured linewidths directly relate to the particle thicknesses along the (hkl) directions. At small momentum transfer $Q < 1.5$ Å^{-1}, Bragg peaks with $k \neq 0$ are negligible (completely absent below 1.0 Å^{-1}) and we therefore estimate the particle lengths L_a, L_c along the a and c directions from simultaneously fitting the $(200)/(101)$ and $(301)/(002)$ peak pairs in the ranges 0.56 Å$^{-1} < Q < 0.95$ Å^{-1} and 1.166 Å$^{-1} < Q < 1.511$ Å^{-1}, respectively. Neglecting any deviations from orthorhombic shape we obtain $L_a \approx t_{200} \approx 6.7\,nm$ and $L_c \approx t_{002} \approx 5.4\,nm$. For the polymer chain length L_b, the fitted integral breadth of the (220) and (121) peaks in the range 1.819 Å$^{-1} < Q < 1.941$ Å^{-1} is clearly smaller than for the peaks orthogonal to the polymer axis, thus indicating $L_b > L_a, L_c$. This is consistent with transmission electron microscopy (Supplementary Figure 11b) showing nanorods with a mean longer axis of $12.5 \pm 4.4\,nm$ and a shorter axis $8.5 \pm 3.4\,nm$ (Supplementary Figure 11c). Based on these results, we assume $L_b \approx 12.5\,nm$.

[Fe(Htrz)$_2$(trz)](BF$_4$) nanorods exhibit a phase transition from the low-temperature LS phase to the high-temperature HS phase in a narrow temperature range around 384-386 K.[18] Supplementary Figure 11d shows a comparison of the room temperature XRD curve $S_{XRD}^{LS}(Q)$ with the calculated LS curve of the compound using the reported *Pnma* crystal structure of the compound,[10] Supplementary Figure 11e shows the measured XRD curve at 395 K ($S_{XRD}^{HS}(Q)$) compared with the calculated HS curve based on the reported HS structure,[10] and Supplementary Figure 11f shows the difference between the high and low temperature XRD curves compared with the calculated HS-LS difference curve. The total scattering signals were calculated using the Debye equation on a ~7 x 13 x 5 nm^3 crystal slab of the LS and HS crystal structures containing 37'434 atoms. Hydrogen atoms were ignored. For both low- and high-temperature measurements, the LS/HS simulations qualitatively reproduce peak positions, widths, and relative intensities, thus confirming the thermally induced phase transition and estimated nanorod linear dimensions.

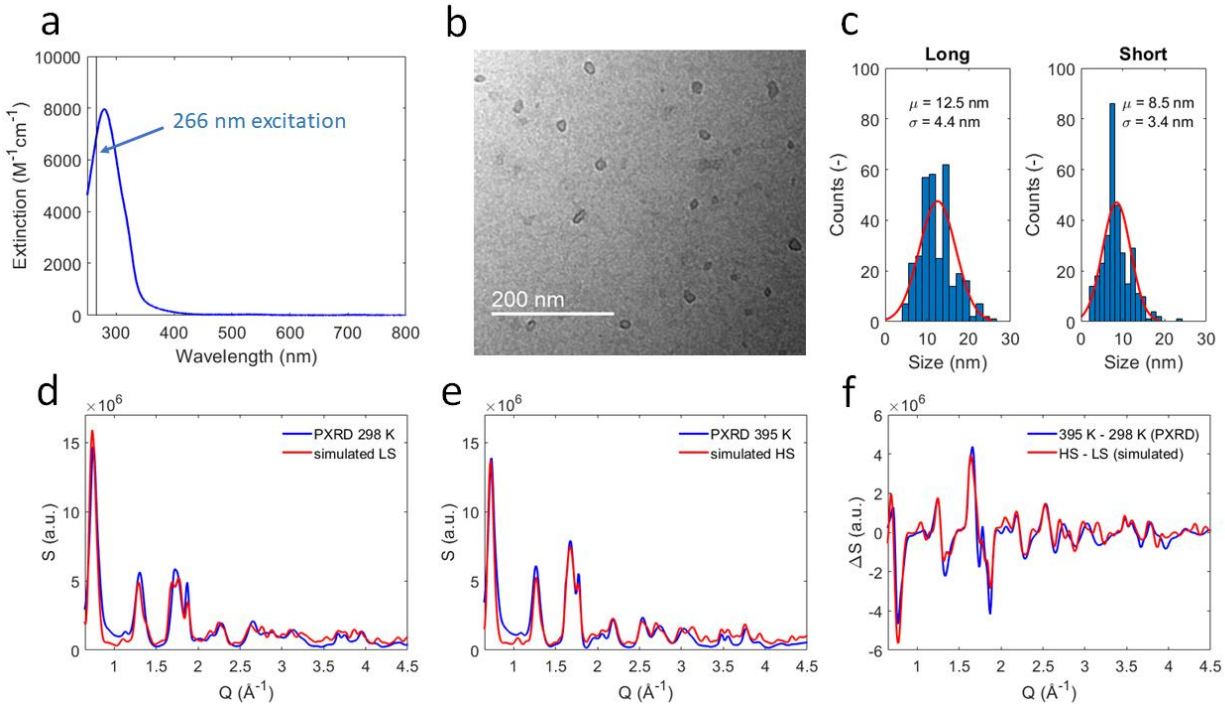

Supplementary Figure 11: (a) Extinction coefficient of Fe-triazole nanorod suspensions in ethanol. The vertical black line indicates the photoexcitation wavelength used in the femtosecond XES/XSS measurements. (b) TEM image of [Fe(Htrz)$_2$(trz)](BF$_4$) nanorods. (c) Distribution of long and short axes determined from TEM images and fitted with normal distributions. (d) Comparison of the measured XRD curve at 298 K and calculated single nanorod X-ray scattering curve from a ~7 x 13 x 5 nm^3 crystal slab of the reported LS crystal structure.[10] (e) Comparison of the measured XRD curve at 395 K and calculated single nanorod X-ray scattering curve from a ~7 x 13 x 5 nm^3 crystal slab of the reported HS crystal structure.[10] (f) Difference of the XRD curves measured at 395/298 K and the calculated HS-LS difference.

Supplementary Note 4: Landau model and volume strain

Hysteretic phase transition, elastic energy and coupling to volume strain: The role of the elastic energy and of the coupling of the ST order parameter to the volume strain was discussed recently on a Landau-based approach.[23-24] The system can be described through the fraction $\gamma = \frac{N_{HS}}{N_{HS}+N_{LS}}$ of HS molecules or through the ST order parameter $q = \frac{N_{HS}-N_{LS}}{N_{HS}+N_{LS}}$, with $q = 2\gamma - 1$, where N_{HS} and N_{LS} denote the number of sites in HS or LS states. The simplest symmetry-adapted Landau potential for describing the hysteretic spin transition in $[Fe(Htrz)_2(trz)](BF_4)$ takes the following form:

$$G(q,T) = A_0(T_c - T)q + \frac{1}{2}B'q^2 + \frac{1}{4}Cq^4 + \lambda_q v_s(\frac{1-q}{2}) + \frac{1}{2}C_s^0 v_s^2 \qquad (16)$$

The q coefficient changes sign at the critical temperature T_c, which balances the stability between HS ($q > 0$) and LS ($q < 0$) states. C>0 is required for stability. $\frac{1}{2}C_s^0 v_s^2$ is the elastic energy related to the elastic constant C_s^0 and the total volume strain, defined as $v_s = \frac{v-v_{HS}}{v_{HS}}$ due to the contraction of volume v from the HS phase volume v_{HS}. $\lambda_q v_s(\frac{1-q}{2})$ is the elastic coupling term of q to v_s and it scales as $(\frac{1-q}{2})$ to be zero in the HS phase. The equilibrium v_s minimizes Supplementary Equation 16:

$$v_s = \frac{\lambda_q}{C_s^0}\left(\frac{q-1}{2}\right) \qquad (17)$$

which highlights that the volume strain scales with the spin transition order parameter q.

Substituting partially v_S in (16) gives:

$$G(q,T) = A_0(T_c - T)q + \frac{1}{2}B'q^2 + \frac{1}{4}Cq^4 + \frac{1}{2}\lambda_q v_s(\frac{1-q}{2}) \qquad (18)$$

$$G(q,T) = (A_0(T_c - T) + \frac{{\lambda_q}^2}{4C_s^0})q + \frac{1}{2}(B' - \frac{{\lambda_q}^2}{4C_s^0})q^2 + \frac{1}{4}Cq^4 - \frac{{\lambda_q}^2}{8C_s^0} \qquad (19)$$

The elastic terms shift the equilibrium line between q<0 and q>0 and decrease the q^2 coefficient. $-\frac{{\lambda_q}^2}{8C_s^0}$ is shifting the origin of energy scale. The Gibbs potential renormalizes to:

$$G(q,T) = A_0(T_{ST} - T)q + \frac{1}{2}Bq^2 + \frac{1}{4}Cq^4 \qquad (20)$$

In the case of a system like $[Fe(Htrz)_2(trz)](BF_4)$, which exhibits a first-order ST curve, the strong elastic coupling makes $B < 0$, which generates 1st order hysteretic spin transition curves centered at T_{ST} from $q = -1$ (γ=0) to $q = 1$ (γ=1), as shown in Supplementary Figure 12.

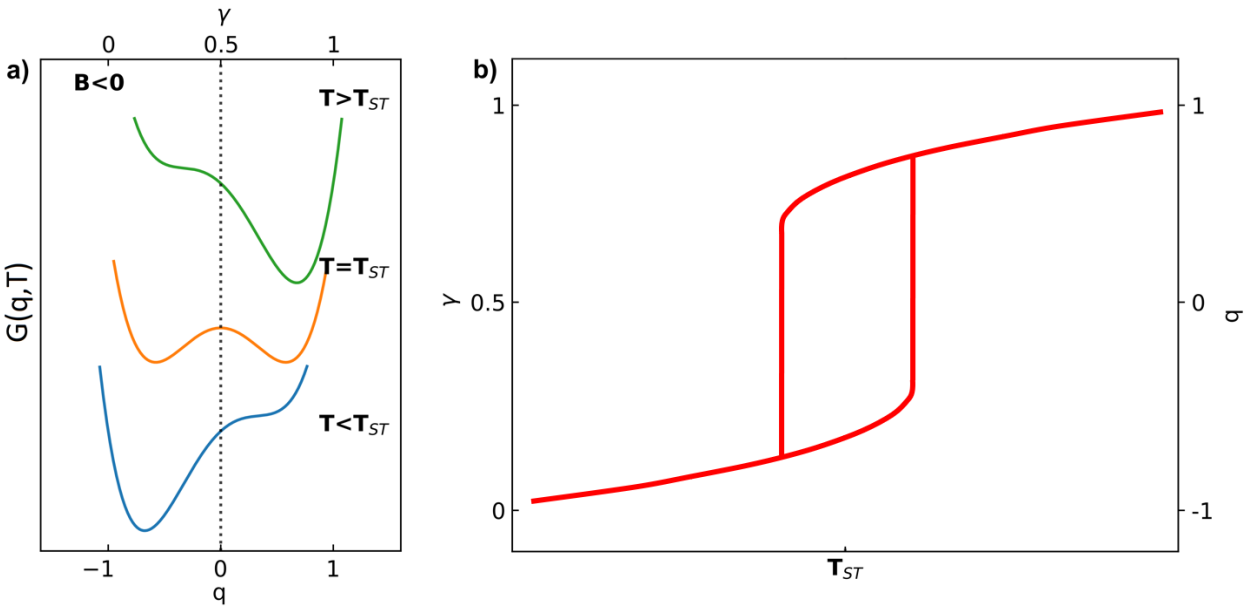

Supplementary Figure 12: (a) Thermal dependence of the Gibbs potential with equilibrium LS ($q < 0$) or HS ($q > 0$) phases. Within thermal hysteresis (e.g., at T_{ST}) both HS and LS states are stable and separated by an energy barrier due to the elastic coupling. (b) The potential in Supplementary Equation 19 gives rise to a hysteretic behavior of the thermal dependence of the ST order parameter q (or HS fraction γ).

Effect of the photoinduced volume expansion and heating: The effect of the volume expansion can be discussed by rewriting Supplementary Equation 18:

$$G(q,T,v_s) = A_0\left(T_c - T - \frac{1}{4}\frac{\lambda_q v_s}{A_0}\right)q + \frac{1}{2}B'q^2 + \frac{1}{4}Cq^4 + \frac{1}{4}\lambda_q v_s \qquad (21)$$

Photodoping increases q and the volume strain, as both are linearly coupled. Indeed, LIESST induces local expansion of Fe-N bonds, corresponding to small polarons and is responsible for volume expansion. Because of the nanometric scale of the nanorods, the photoexcitation is homogeneous and v_s, modified by HS photodoping, equilibrates within few ps. Consequently, we can consider that on this timescale, where elastic degrees of freedom get equilibrated through the change of the volume strain, photodoping elastically modifies the equilibrium along the Gibbs potential, as shown in Figure 4. The volume expansion dv_s due to photodoping renormalizes T_{ST} and stabilizes the HS state. Supplementary Figure 13 shows that dv_s, induced by photodoping, results in a relative stabilization of the HS state with respect to the LS state.

Following the photodoping process, the excess vibrational energy redistribution gives rise to a temperature increase, which is estimated to $dT \approx 60\ K$ at the photodoping threshold $\gamma_{th} \approx 16\%$, above which the ST occurs (Supplementary Note 2). A temperature rise also stabilizes the HS state of higher entropy. However, the equilibration timescale, for which temperature can be defined for the Gibbs potential when all degrees of freedom are equilibrated, may be slower as

the system needs time to explore HS-LS configuration equilibrium. This may be the origin of the incubation period t_1 prior to a secondary completion of the nanorod phase transition within τ_1.

In the case of high photodoping, the volume expansion is larger. This fully destabilizes the LS state, as shown in the upper left panel of Figure 4, and the energy barrier towards the HS state vanishes. The system then relaxes directly towards the HS state.

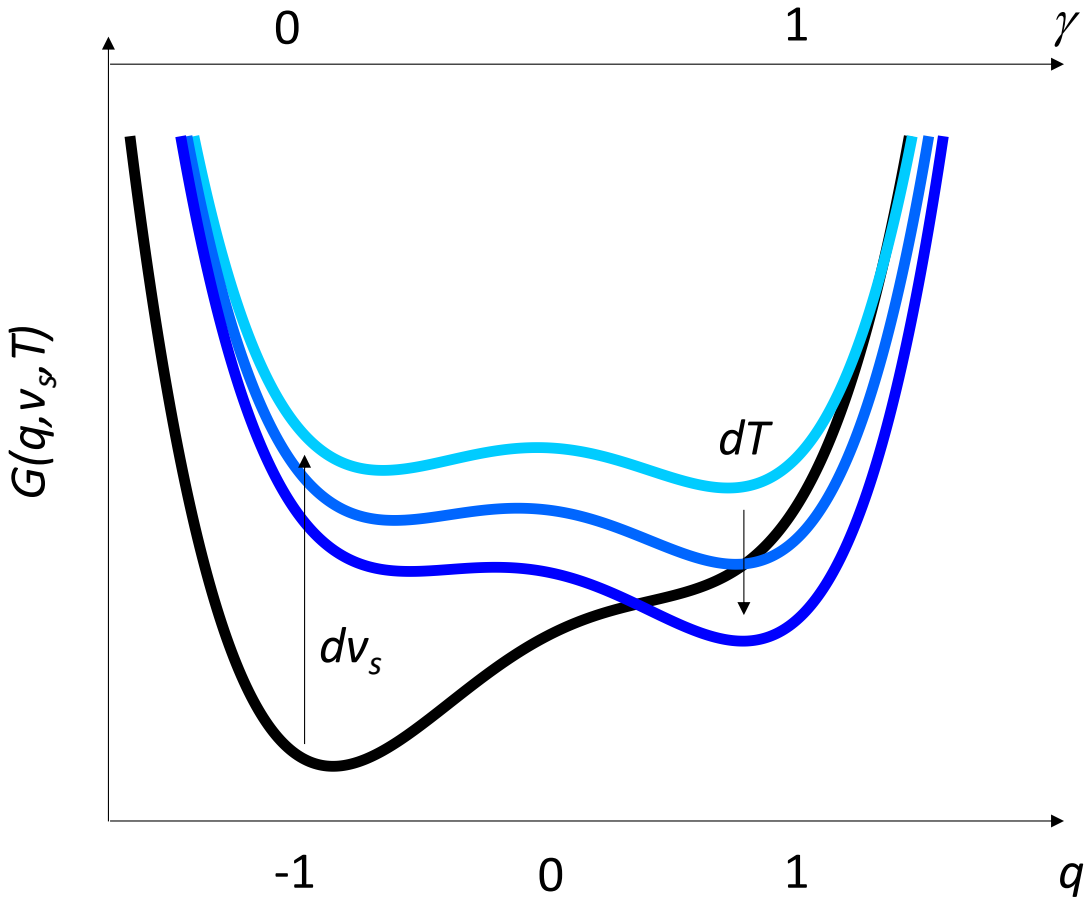

Supplementary Figure 13: Photodoping is responsible for a variation of the volume strain dv_s, which destabilizes the LS state and stabilizes the HS state. This modification occurs on the equilibration timescale of the elastic degrees of freedom. A temperature rise (dT) can further balance this relative stability of the HS state.

Supplementary Note 5: Extraction of unit cell dimensions from the excited state scattering curves

We have also extracted lattice parameters using a profile matching procedure with constant scale factor as implemented in the FullProf software.[25] These fits utilize the *Pnma* space group reported for the compound,[10] with lattice angles fixed to 90 degrees. Deviation of lattice angles from 90 degrees would give rise to a ferroelastic phase transition towards monoclinic or triclinic lattices characterized by the splitting of Bragg peaks, which is not observed here. The FWHM and shape parameters were fixed to zero except for the shape parameter SZ that is determined by the particle size. The nanorod size was considered by including three coefficients of the anisotropic Lorentzian size broadening model in the fit. The resulting average apparent size is consistent with the nanorod size estimate in Supplementary Note 3. Similar spherical harmonics coefficients were obtained for the LS and HS phases and then used to analyze the time-resolved data. All fits were performed by including a few background points that were optimized together with the lattice spacings. This procedure yielded stable and satisfactory fits and we did therefore not attempt to extract and analyze any potential subtle time-dependent changes in peak widths unrelated with the nanorod size. As outlined in Supplementary Note 2, we do not expect a reliable separation of the *a*- and *c*-spacings and therefore only report their product $\sigma_\perp = a \cdot c$. The resulting structural parameters for the thermal equilibrium LS and HS phases are in good agreement with values reported by Grosjean et al.[10] and shown in Supplementary Table 2.

Excitation fluence (mJ/cm^2)	b (Å)	$\sigma_\perp = a \times c$ (Å^2)	$v = a \times b \times c$ (Å^3)
LS	7.33 (7.32)	160 (159)	1170 (1167)
HS	7.77 (7.79)	171 (167)	1332 (1303)
HS - LS	0.44 (0.47)	11 (8)	162 (136)

Supplementary Table 2: Extracted structural parameters for the LS and HS X-ray diffraction curves measured at thermal equilibrium. Reported values from Grosjean et al. at thermal equilibrium are shown in brackets.[10]

Supplementary Figure 14 shows the time-dependent structural parameters b, $\sigma_\perp$ and the volume strain $v_s = \frac{v - v_{HS}}{v_{HS}}$ (Supplementary Note 4) for excitation fluences of 35 mJ/cm^2 and 70 mJ/cm^2. The observed time-evolution of the lattice parameters resembles the time-dependent peak positions shown in Figure 3 (Supplementary Note 2) but was determined with coarser time bins. The nanorod cross section $\sigma_\perp$ expands within ~1.5 ps while the b-spacing expands on a slower ~4 ps timescale. During the incubation period, the lattice structure does not significantly evolve but during the secondary spin conversion step, the increase in the *b*-spacing is delayed with respect to $\sigma_\perp$. We expect that the time-evolution of the unit cell dimensions predominantly reflects changes in the spin population while the impact of ordinary thermal expansion is likely less pronounced.[26]

Supplementary Figure 15 shows the time-dependent normalized intensity I/I_0 for two selected Bragg peaks at 35/70 mJ/cm^2. For both fluences, the (101)-peak intensity decreases within ~1.5

ps, the expansion timescale orthogonal to the chain axis. Along the (121)-peak direction, the intensity decreases within ~4 ps, concomitant with the observed expansion timescale along this direction. Overall, these curves do not exhibit a monotonous decrease in normalized intensity that could be associated with an increase in the nanorod temperature. For the (121)-peak, the decrease in intensity after ~60 ps is larger for the lower excitation fluence (35 mJ/cm^2) than for the higher fluence (70 mJ/cm^2). This further indicates that these peak intensities may be dominated by intramolecular structure changes due to the photoinduced low-spin to high-spin conversion rather than temperature effects. These considerations highlight the limits of our analysis in tracking vibrational excess energy dissipation within the nanorods.

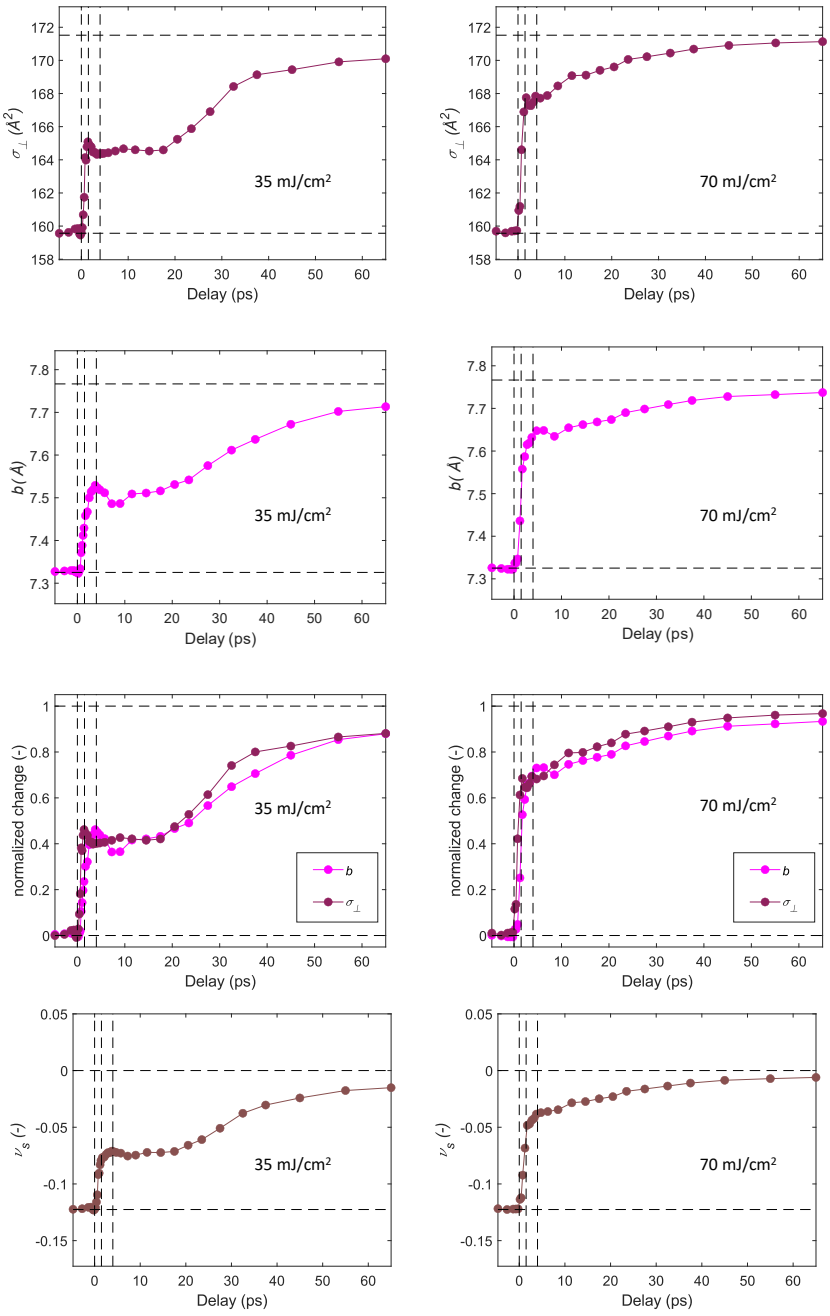

Supplementary Figure 14: Time-dependent unit cell parameters $\sigma_{\perp}$ and b extracted from X-ray scattering data collected with excitation fluences of 35 mJ/cm^2 (left column) and 70 mJ/cm^2 (right column). Vertical black dashed lines are shown at 0 ps, 1.5 ps and 4 ps. The insets in the third row show curves normalized to the HS-LS difference from Supplementary Table 2. The fourth row shows the associated photoinduced volume strain v_s.

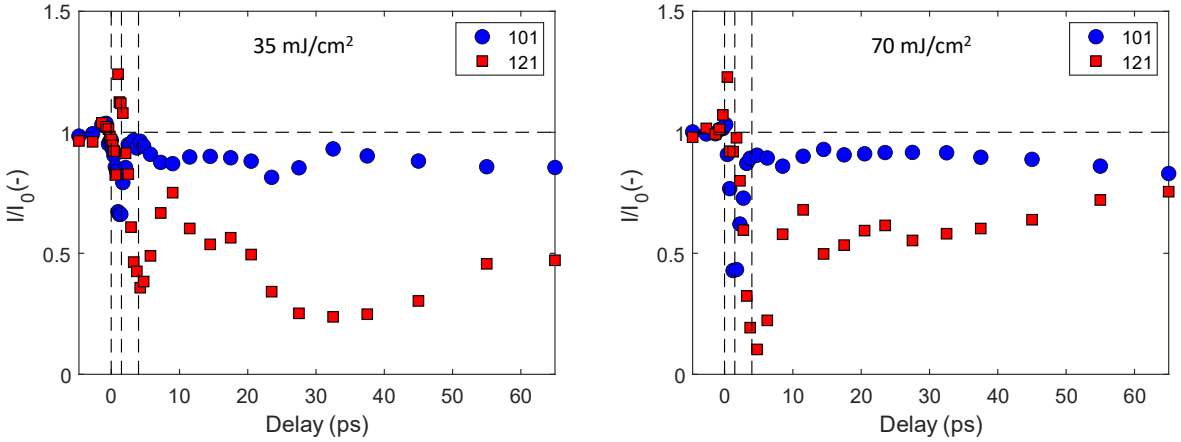

Supplementary Figure 15: Time-dependent normalized intensity (I/I_0) for two different Bragg peaks shown for excitation fluences of 35 mJ/cm^2 and 70 mJ/cm^2. I_0 was calculated as the average peak intensity before -0.3 ps.

References

1. Zhang, W.; Alonso-Mori, R.; Bergmann, U.; Bressler, C.; Chollet, M.; Galler, A.; Gawelda, W.; Hadt, R. G.; Hartsock, R. W.; Kroll, T.; Kjaer, K. S.; Kubicek, K.; Lemke, H. T.; Liang, H. W.; Meyer, D. A.; Nielsen, M. M.; Purser, C.; Robinson, J. S.; Solomon, E. I.; Sun, Z.; Sokaras, D.; van Driel, T. B.; Vanko, G.; Weng, T.-C.; Zhu, D.; Gaffney, K. J., Tracking excited-state charge and spin dynamics in iron coordination complexes. *Nature* **2014,** *509* (7500), 345-348.
2. Zhang, K.; Ash, R.; Girolami, G. S.; Vura-Weis, J., Tracking the Metal-Centered Triplet in Photoinduced Spin Crossover of Fe(phen)32+ with Tabletop Femtosecond M-Edge X-ray Absorption Near-Edge Structure Spectroscopy. *Journal of the American Chemical Society* **2019,** *141* (43), 17180-17188.
3. Fouché, O.; Degert, J.; Jonusauskas, G.; Baldé, C.; Desplanche, C.; Létard, J. F.; Freysz, E., Laser induced spin state transition: Spectral and temporal evolution. *Chemical Physics Letters* **2009,** *469* (4), 274-278.
4. Auböck, G.; Chergui, M., Sub-50-fs photoinduced spin crossover in [Fe(bpy)3]2+. *Nat Chem* **2015,** *7* (8), 629-633.
5. Bressler, C.; Milne, C.; Pham, V.-T.; ElNahhas, A.; van der Veen, R. M.; Gawelda, W.; Johnson, S.; Beaud, P.; Grolimund, D.; Kaiser, M.; Borca, C. N.; Ingold, G.; Abela, R.; Chergui, M., Femtosecond XANES Study of the Light-Induced Spin Crossover Dynamics in an Iron(II) Complex. *Science* **2009,** *323* (5913), 489-492.
6. Cannizzo, A.; Milne, C. J.; Consani, C.; Gawelda, W.; Bressler, C.; van Mourik, F.; Chergui, M., Light-induced spin crossover in Fe(II)-based complexes: The full photocycle unraveled by ultrafast optical and X-ray spectroscopies. *Coordination Chemistry Reviews* **2010,** *254* (21), 2677-2686.
7. Kjær, K. S.; Van Driel, T. B.; Harlang, T. C. B.; Kunnus, K.; Biasin, E.; Ledbetter, K.; Hartsock, R. W.; Reinhard, M. E.; Koroidov, S.; Li, L.; Laursen, M. G.; Hansen, F. B.; Vester, P.; Christensen, M.; Haldrup, K.; Nielsen, M. M.; Dohn, A. O.; Pápai, M. I.; Møller, K. B.; Chabera, P.; Liu, Y.; Tatsuno, H.; Timm, C.; Jarenmark, M.; Uhlig, J.; Sundstöm, V.; Wärnmark, K.; Persson, P.; Németh, Z.; Szemes, D. S.; Bajnóczi, É.; Vankó, G.; Alonso-Mori, R.; Glownia, J. M.; Nelson, S.; Sikorski, M.; Sokaras, D.; Canton, S. E.; Lemke, H. T.; Gaffney, K. J., Finding intersections between electronic excited state potential energy surfaces with simultaneous ultrafast X-ray scattering and spectroscopy. *Chemical Science* **2019,** *10* (22), 5749-5760.
8. Hauser, A., Light-Induced Spin Crossover and the High-Spin→Low-Spin Relaxation. In *Spin Crossover in Transition Metal Compounds II*, Gütlich, P.; Goodwin, H. A., Eds. Springer Berlin Heidelberg: Berlin, Heidelberg, 2004; pp 155-198.
9. Field, R.; Liu, L. C.; Gawelda, W.; Lu, C.; Miller, R. J. D., Spectral Signatures of Ultrafast Spin Crossover in Single Crystal [FeII(bpy)3](PF6)2. *Chemistry – A European Journal* **2016,** *22* (15), 5118-5122.
10. Grosjean, A.; Négrier, P.; Bordet, P.; Etrillard, C.; Mondieig, D.; Pechev, S.; Lebraud, E.; Létard, J.-F.; Guionneau, P., Crystal Structures and Spin Crossover in the Polymeric Material [Fe(Htrz)2(trz)](BF4) Including Coherent-Domain Size Reduction Effects. *European Journal of Inorganic Chemistry* **2013,** *2013* (5-6), 796-802.
11. Kjaer, K. S.; van Driel, T. B.; Kehres, J.; Haldrup, K.; Khakhulin, D.; Bechgaard, K.; Cammarata, M.; Wulff, M.; Sorensen, T. J.; Nielsen, M. M., Introducing a standard method for experimental determination of the solvent response in laser pump, X-ray probe time-resolved wide-angle X-ray scattering experiments on systems in solution. *Physical Chemistry Chemical Physics* **2013,** *15* (36), 15003-15016.
12. Reinhard, M.; Gallo, A.; Guo, M.; Garcia-Esparza, A. T.; Biasin, E.; Qureshi, M.; Britz, A.; Ledbetter, K.; Kunnus, K.; Weninger, C.; van Driel, T.; Robinson, J.; Glownia, J. M.; Gaffney, K. J.; Kroll, T.; Weng, T.-C.; Alonso-Mori, R.; Sokaras, D., Ferricyanide photo-aquation pathway revealed by combined

femtosecond Kβ main line and valence-to-core x-ray emission spectroscopy. *Nature Communications* **2023,** *14* (1), 2443.
13. Reinhard, M. E.; Mara, M. W.; Kroll, T.; Lim, H.; Hadt, R. G.; Alonso-Mori, R.; Chollet, M.; Glownia, J. M.; Nelson, S.; Sokaras, D.; Kunnus, K.; Driel, T. B. v.; Hartsock, R. W.; Kjaer, K. S.; Weninger, C.; Biasin, E.; Gee, L. B.; Hodgson, K. O.; Hedman, B.; Bergmann, U.; Solomon, E. I.; Gaffney, K. J., Short-lived metal-centered excited state initiates iron-methionine photodissociation in ferrous cytochrome c. *Nature Communications* **2021,** *12* (1), 1086.
14. Park, S. T.; Veen, R. M. v. d., Modeling nonequilibrium dynamics of phase transitions at the nanoscale: Application to spin-crossover. *Structural Dynamics* **2017,** *4* (4), 044028.
15. Roubeau, O.; Castro, M.; Burriel, R.; Haasnoot, J. G.; Reedijk, J., Calorimetric Investigation of Triazole-Bridged Fe(II) Spin-Crossover One-Dimensional Materials: Measuring the Cooperativity. *The Journal of Physical Chemistry B* **2011,** *115* (12), 3003-3012.
16. Kroeber, J.; Audiere, J.-P.; Claude, R.; Codjovi, E.; Kahn, O.; Haasnoot, J. G.; Groliere, F.; Jay, C.; Bousseksou, A., Spin Transitions and Thermal Hysteresis in the Molecular-Based Materials [Fe(Htrz)2(trz)](BF4) and [Fe(Htrz)3](BF4)2.cntdot.H2O (Htrz = 1,2,4-4H-triazole; trz = 1,2,4-triazolato). *Chemistry of Materials* **1994,** *6* (8), 1404-1412.
17. Lefter, C.; Tricard, S.; Peng, H.; Molnár, G.; Salmon, L.; Demont, P.; Rotaru, A.; Bousseksou, A., Metal Substitution Effects on the Charge Transport and Spin Crossover Properties of [Fe1–xZnx(Htrz)2(trz)](BF4) (trz = Triazole). *The Journal of Physical Chemistry C* **2015,** *119* (16), 8522-8529.
18. Coronado, E.; Galán-Mascarós, J. R.; Monrabal-Capilla, M.; García-Martínez, J.; Pardo-Ibáñez, P., Bistable Spin-Crossover Nanoparticles Showing Magnetic Thermal Hysteresis near Room Temperature. *Advanced Materials* **2007,** *19* (10), 1359-1361.
19. Dugay, J.; Giménez-Marqués, M.; Kozlova, T.; Zandbergen, H. W.; Coronado, E.; van der Zant, H. S. J., Spin Switching in Electronic Devices Based on 2D Assemblies of Spin-Crossover Nanoparticles. *Advanced Materials* **2015,** *27* (7), 1288-1293.
20. Gimenez-Marques, M.; Garcia-Sanz de Larrea, M. L.; Coronado, E., Unravelling the chemical design of spin-crossover nanoparticles based on iron(ii)-triazole coordination polymers: towards a control of the spin transition. *Journal of Materials Chemistry C* **2015,** *3* (30), 7946-7953.
21. Sherwood, D.; Emmanuel, B., Computing Shapes of Nanocrystals from X-ray Diffraction Data. *Crystal Growth & Design* **2006,** *6* (6), 1415-1419.
22. Langford, J. I.; Wilson, A. J. C., Scherrer after sixty years: A survey and some new results in the determination of crystallite size. *Journal of Applied Crystallography* **1978,** *11* (2), 102-113.
23. Collet, E.; Azzolina, G., Coupling and decoupling of spin crossover and ferroelastic distortion: Unsymmetric hysteresis loop, phase diagram, and sequence of phases. *Physical Review Materials* **2021,** *5* (4), 044401.
24. Azzolina, G.; Bertoni, R.; Collet, E., General Landau theory of non-symmetry-breaking and symmetry-breaking spin transition materials. *Journal of Applied Physics* **2021,** *129* (8).
25. Rodriguez-Carvajal, J., Recent developments of the program FULLPROF, commission on powder diffraction. *IUCr Newsl.* **2001,** *26*.
26. Paliwoda, D.; Vendier, L.; Getzner, L.; Alabarse, F.; Comboni, D.; Martin, B.; Alavi, S. E.; Bello, M. P.; Salmon, L.; Nicolazzi, W.; Molnár, G.; Bousseksou, A., Elastic Properties of the Iron(II)–Triazole Spin Crossover Complexes [Fe(Htrz)2trz]BF4 and [Fe(NH2trz)3]SO4. *Crystal Growth & Design* **2023,** *23* (3), 1903-1914.